A High-Resolution Spectroscopic Survey of Directly Imaged Companion Hosts
I. Determination of diagnostic stellar abundances for planet formation and composition

ANEESH BABURAJ,[1,2] QUINN M. KONOPACKY,[1] CHRISTOPHER A. THEISSEN,[1] SARAH PEACOCK,[3,4] LORI HUSEBY,[5]
BENJAMIN FULTON,[6] ROMAN GERASIMOV,[7] TRAVIS S. BARMAN,[5] AND KIELAN K. W. HOCH[8]

✔ 直接撮像されている惑星と主星の組成比を調べることで惑星形成を制約できる

- 重力不安定でできたのなら組成比はあまり変わらない
- コア形成モデルなら、形成した場所で組成比が変わる

✔ この論文では5つの直接撮像されている天体について主星の組成比を調べた。

- Automated Planet Finder (Lick Observatory), 2.4 m
- Levy optical echelle spectrometer (R=130,000, 374–900n)

Table 1. Observing schedule for targets in this work

Target	Number of frames	Integration Time per frame (s)	Observation date (UT)	Total Int. Time (s)
HIP 25278 [a]	1	148	December 27, 2016	148
51 Eri	1	54	August 26, 2015	54
HR 8799	1	300	July 29, 2015	300
HD 984	1	997	November 6, 2015	997
GJ 504	4	25	February 27, 2021	100
HD 206893	1	900	August 7, 2023	3600
	1	900	August 9, 2023	
	1	900	August 25, 2023	
	1	900	August 26, 2023	

パラメータ推定

✔ 恒星大気モデルによるフィッティング

- PHOENIX (Husser+2013)を使用。Teff, log g, [M/H]が基本パラメータ
- モデルを拡張して、[C/H], [O/H]もパラメータとして加えた (PHOENIX-C/O)

We identified several stellar absorption lines that could be used for the estimation of carbon and oxygen abundances, and subsequently the C/O ratio. For carbon, we use the C I lines at 4772, 4932, 5052, 5380, and 6587 Å. Obtaining the oxygen abundance is more difficult due to the lack of easily detectable atomic oxygen features in the optical region of the stellar spectrum as well as other complications (e.g., blends, three-dimensional, non-LTE effects) (Asplund 2005). In the optical region, the only lines present are the forbidden [O I] line at 6300 Å (which is low-excitation and very sensitive to minor changes in the stellar atmospheric temperature; Asplund 2005) and the O I triplet lines at 6155–58 and 7771–75 Å. These lines are usually present for stars of spectral types BAFGK, which applies to the stars in our dataset (Takeda & Takada-Hidai 2013). For the remaining 13 elements (Na, Mg, Si, S, Ca, Sc, Ti, Cr, Mn, Fe, Ni, Zn,

✔ Telluricと恒星大気の同時モデリング

$$D[p] = C \times \left[\left(M\left[p(\lambda[1+\frac{RV}{c}]), T_{\rm eff}, \log g, [M/H] \right] \otimes \kappa_R(v \sin i) \right) \times T\left[p(\lambda), altitude, pwv \right]^{\alpha} \right] \otimes \kappa_R(\Delta\nu_{inst}) + C_{flux} \quad (3)$$

- 恒星大気 (PHOENIX) で同時モデリングしたのち、その結果をpriorとして PHOENIX-C/Oで再度モデリング

51 Eri

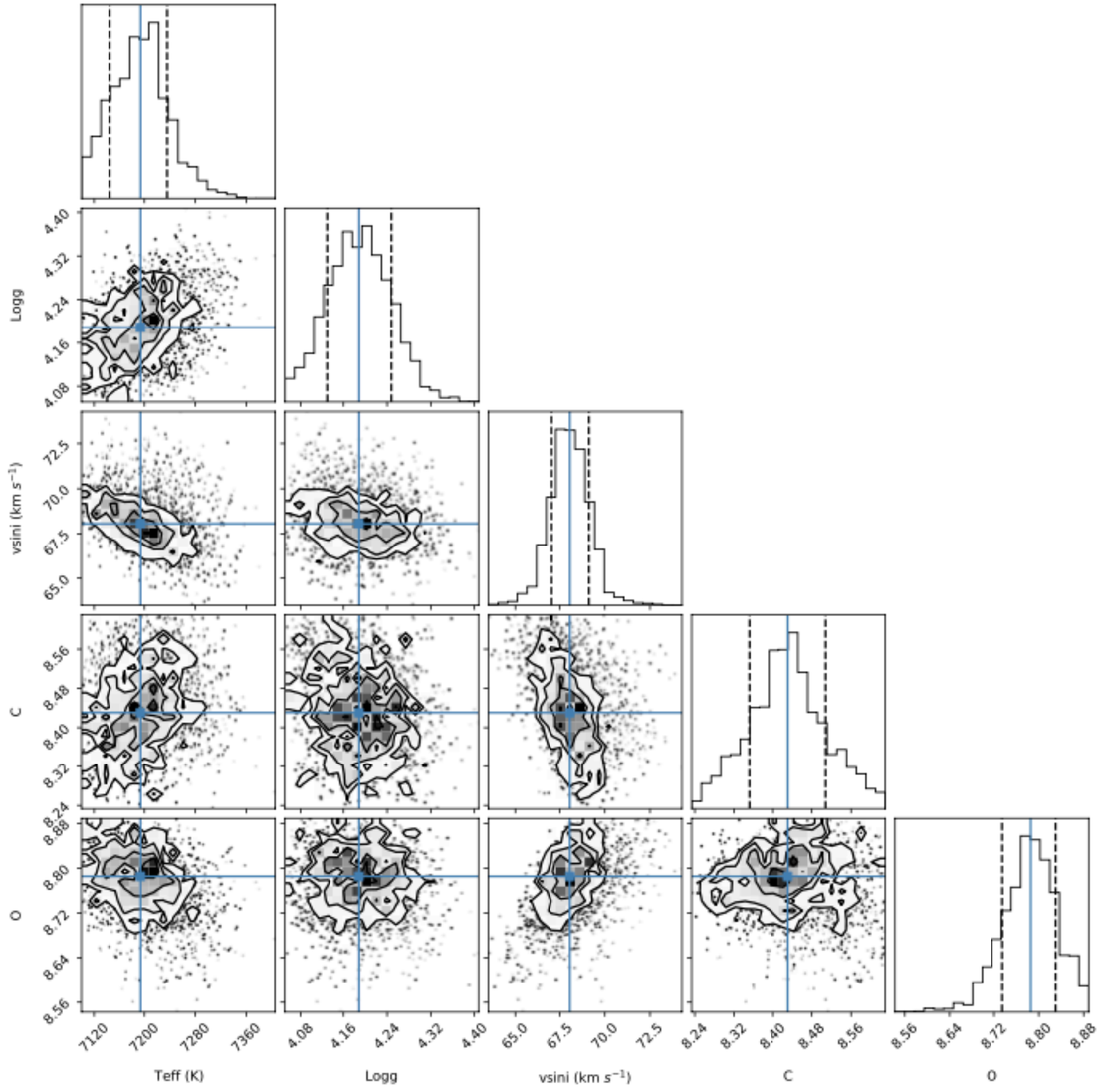
Teff (K)
Logg
vsini (km s^{-1})
C
O

C I

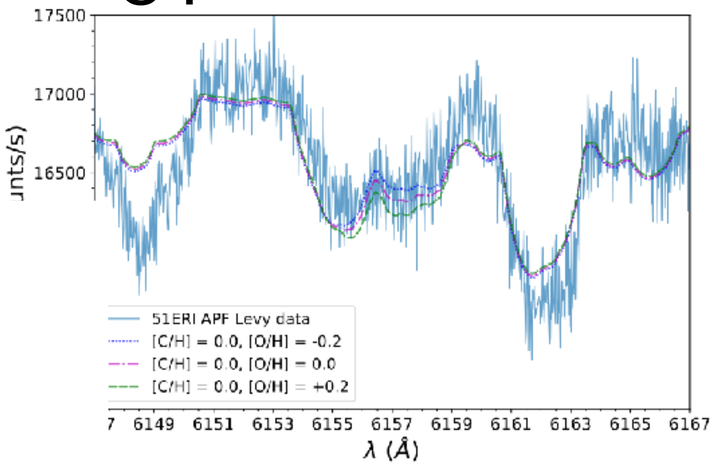
51ERI APF Levy data
[C/H] = 0.0, [O/H] = -0.2
[C/H] = 0.0, [O/H] = 0.0
[C/H] = 0.0, [O/H] = +0.2
λ (Å)

O I

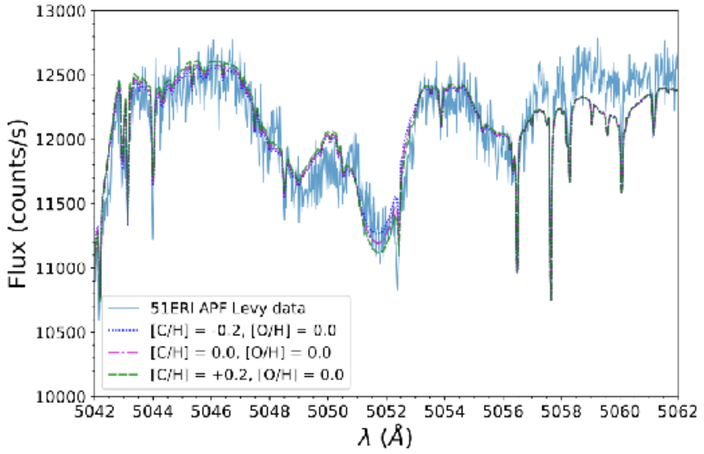
Flux (counts/s)
51ERI APF Levy data
[C/H] = 0.2, [O/H] = 0.0
[C/H] = 0.0, [O/H] = 0.0
[C/H] = +0.2, [O/H] = 0.0
λ (Å)

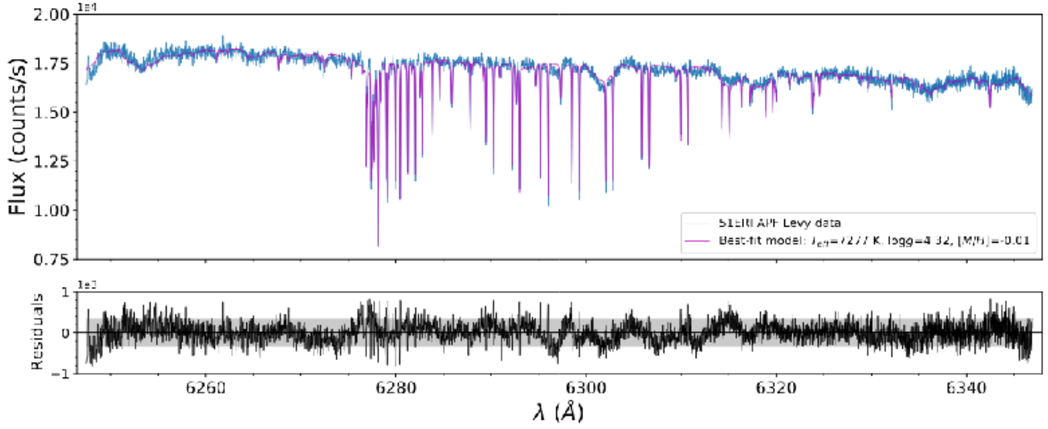
Flux (counts/s)
Residuals
λ (Å)

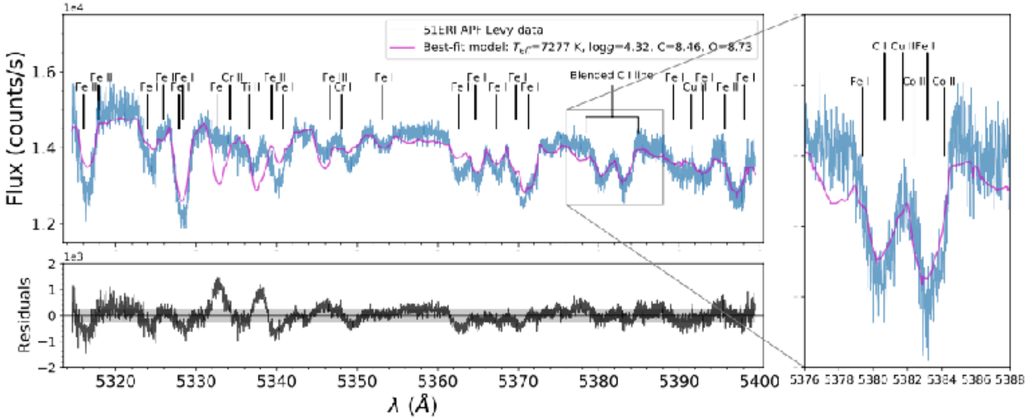
Flux (counts/s)
Residuals
λ (Å)

惑星-主星のC/O比の比較

Target	Work	$T_{\rm eff}$ (K)	log g (cgs)	[M/H]	[C/H]	[O/H]
51 Eri	This work	7277 ± 164	4.32 ± 0.23	-0.01 ± 0.11	0.03 ± 0.08 [a] -0.02 ± 0.16 [b]	0.04 ± 0.08 [a] -0.01 ± 0.17 [b]
	Saffe et al. (2021)	7259 ± 167	4.12 ± 0.20	-0.06 ± 0.10		
	Arentsen et al. (2019)	7366 ± 146	4.09 ± 0.21	0.09 ± 0.07		
	Luck (2017)	7146 ± 62	4.23	0.24 ± 0.35		
	Koleva & Vazdekis (2012)	7414 ± 31	4.09 ± 0.13	-0.02 ± 0.08		
HR 8799	This work	7317 ± 176	4.32 ± 0.20	-0.57 ± 0.08	0.13 ± 0.04 [a] 0.04 ± 0.19 [b]	0.10 ± 0.07 [a] 0.11 ± 0.20 [b]
	Saffe et al. (2021)	7301 ± 190	4.12 ± 0.23	-0.70 ± 0.15		
	Wang et al. (2020)	7390 ± 80	4.35 ± 0.07	-0.52 ± 0.08	0.11 ± 0.12	0.12 ± 0.14
	Sadakane (2006)	7250	4.30	-0.50	0.20	0.19
	Gray et al. (2003)	7422	4.22	-0.50		
HD 984	This work	6401 ± 177	4.42 ± 0.16	-0.01 ± 0.09	0.06 ± 0.07 [a] 0.04 ± 0.09 [b]	0.00 ± 0.07 [a] 0.10 ± 0.24 [b]
	Costes et al. (2024)			-0.01 ± 0.12	-0.05 ± 0.10	0.09 ± 0.20
	Rice & Brewer (2020)	6479 ± 42	4.43 ± 0.05	0.06 ± 0.02		
	Luck (2018)	6266 ± 24	4.31	0.27		
	Valenti & Fischer (2005)	6490	4.83	-0.05		
GJ 504 [c]	This work	5959 ± 145	4.65 ± 0.33	0.12 ± 0.08	0.27 ± 0.03 [a] 0.35 ± 0.19 [b]	0.28 ± 0.11 [a] 0.47 ± 0.16 [b]
	Hirsch et al. (2021)	6080 ± 100	4.3 ± 0.1	0.21 ± 0.06		
	D'Orazi et al. (2017)	6205 ± 20	4.29 ± 0.07	0.22 ± 0.04	-0.004 ± 0.109	0.030 ± 0.059
HD 206893	This work	6617 ± 46	4.27 ± 0.15	0.06 ± 0.18	0.14 ± 0.03 [a] 0.12 ± 0.16 [b]	-0.03 ± 0.07 [a] 0.02 ± 0.15 [b]
	Zakhozhay et al. (2022)	6680	4.34	0.08		
	Delorme et al. (2017)	6500 ± 100	4.45 ± 0.15	0.04 ± 0.02		
	Maldonado et al. (2012)			-0.01		

[a] Abundances obtained using spectral fitting.

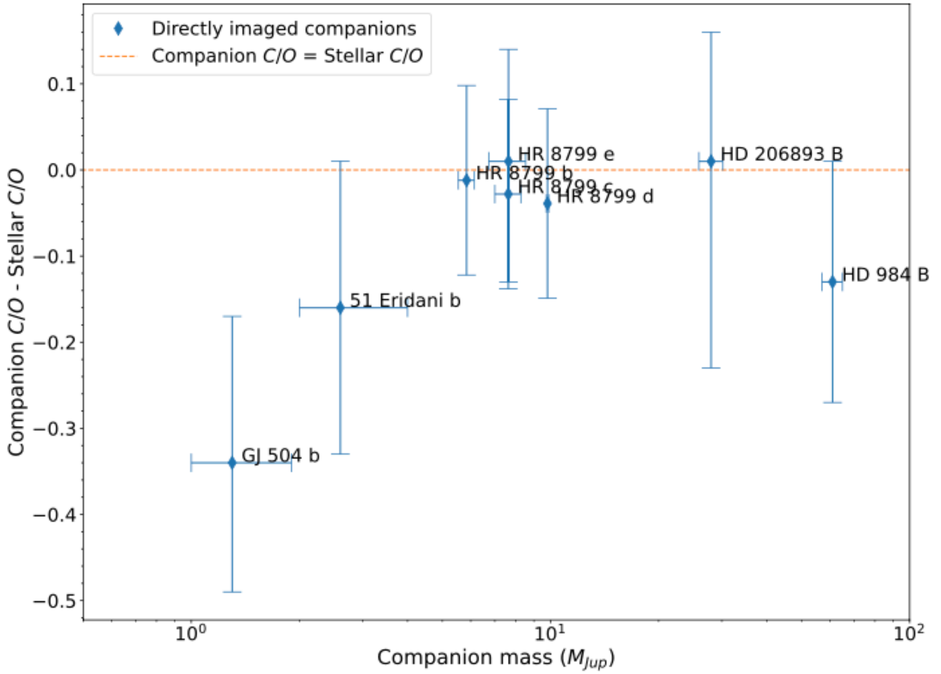

Table 8. Companion masses and C/O ratios

Companion	Mass ($M_{\rm Jup}$)	C/O Ratio	References
51 Eri b	≤11 (Dynamical) 2–9 (Evolutionary)	0.38 ± 0.09	1, 2, 3, 4, 5, 6, 7, 8
HR 8799 b	5.84 ± 0.3	$0.578^{+0.004}_{-0.005}$	9, 10, 11
HR 8799 c	$7.63^{+0.64}_{-0.63}$	0.562 ± 0.004	9, 10, 11
HR 8799 d	9.81 ± 0.08	$0.551^{+0.005}_{-0.004}$	9, 10, 11
HR 8799 e	$7.64^{+0.89}_{-0.91}$	$0.60^{+0.07}_{-0.08}$	9, 10, 12
HD 984 B	61 ± 4	0.50 ± 0.01	13, 17
GJ 504 b	$1.3^{+0.6}_{-0.3}$ (Young system) 23.0^{+10}_{-9} (Old system)	$0.20^{+0.09}_{-0.06}$	14
HD 206893 B	$28.0^{+2.2}_{-2.1}$	0.65–0.90	15, 16
HD 206893 c	$12.7^{+1.2}_{-1.0}$		15

References—(1) De Rosa et al. (2020), (2) Dupuy et al. (2022), (3) Macintosh et al. (2015), (4) Samland et al. (2017), (5) Nielsen et al. (2019), (6) Brown-Sevilla et al. (2023), (7) Whiteford et al. (2023), (8) Elliott et al. (2024), (9) Sepulveda & Bowler (2022), (10) Zurlo et al. (2022), (11) Ruffio et al. (2021), (12) Mollière et al. (2020), (13) Franson et al. (2022), (14) Bonnefoy et al. (2018), (15) Hinkley et al. (2023), (16) Kammerer et al. (2021), (17) Costes et al. (2024)

✔ **GJ 504 bのみ大きな差異が見られた。**

✔JWSTによるさらなる観測が予定されている

- C/S, O/Sなどが制約されることが期待

Dusty substructures induced by planets in ALMA disks: how dust growth and dynamics changes the picture

Alexandros Ziampras[1]*, Prakruti Sudarshan[2]†, Cornelis P. Dullemond[3], Mario Flock[2], Vittoria Berta[4], Richard P. Nelson[1], Andrea Mignone[4]

[1]*Astronomy Unit, School of Physics and Astronomy, Queen Mary University of London, London E1 4NS, UK*
[2]*Max-Planck-Institut für Astronomie, Königstuhl 17, 69117 Heidelberg, Germany*
[3]*Institute for Theoretical Astrophysics, Center for Astronomy (ZAH), Heidelberg University, Albert Ueberle Str. 2, 69120 Heidelberg, Germany*
[4]*Dipartimento di Fisica, Università di Torino, via Pietro Giuria 1, 10125 Torino, Italy*

✔ ギャップ形成におけるdust dynamicsの役割を知りたい

- opacity feedback, back reactionによる影響を調べた

- 一般的にcoolingがよく効く -> ギャップが深くなる (惑星に物が落ちやすくなるから?)

✔ 2Dの輻射流体計算を行った

- PLUTO (Mignone+2007)
- 2.04Msun, 16.98Lsun (HD 163296)

$$\Sigma_{g,0} = 10\,\mathrm{g/cm^2}\left(\frac{R}{R_0}\right)^{-1}, \quad T_0 = 34.64\,K\left(\frac{R}{R_0}\right)^{-3/7}$$

R0 = 48 au

ガス

$$\frac{d\Sigma_g}{dt} = -\Sigma_g \nabla \cdot \boldsymbol{u}_g,$$

$$\Sigma_g \frac{d\boldsymbol{u}_g}{dt} = -\nabla P - \Sigma_g \nabla \Phi + \nabla \cdot \overline{\sigma}, \qquad \Phi = \Phi_\star + \Phi_p,$$

$$\frac{de}{dt} = -\gamma e \nabla \cdot \boldsymbol{u}_g + Q_{visc} + Q_{irr} + Q_{cool} + Q_{rad},$$

(α~10^-6, 乱流はほぼ無視)

ダスト

$$\frac{d\Sigma_d}{dt} = -\Sigma_d \nabla \cdot \boldsymbol{u}_d,$$

$$\Sigma_d \frac{d\boldsymbol{u}_d}{dt} = -\Sigma_d \nabla \Phi - \Sigma_d \frac{\boldsymbol{u}_d - \boldsymbol{u}_g}{St} \Omega_K,$$

ダスト->ガスのフィードバック

$$\Sigma_g \frac{\partial \boldsymbol{u}_g}{\partial t} = -\Sigma_d \frac{\boldsymbol{u}_g - \boldsymbol{u}_d}{St} \Omega_K.$$

２種のダスト分布、ダストフィードバック

✔ ダストとして、小さいダスト”0.1um”と大きいダスト”1mm”の二種類を考える

- 小さいダストはガスとcouple
- 大きいダストは運動する

$$\kappa_{\rm R,P} = \frac{\kappa_{\rm R,P}^{\rm small}\Sigma_{\rm d}^{\rm small} + \kappa_{\rm R,P}^{\rm big}\Sigma_{\rm d}^{\rm big}}{\Sigma_{\rm d}^{\rm small} + \Sigma_{\rm d}^{\rm big}} = (1-X)\,\kappa_{\rm R,P}^{\rm small} + X\,\kappa_{\rm R,P}^{\rm big},$$

$$\kappa_{\rm R}^{\rm small} \approx 0.27\,T_{\rm K}^{1.6}\,{\rm cm}^2/{\rm g}, \quad \kappa_{\rm P}^{\rm small} \approx 0.41\,T_{\rm K}^{1.6}\,{\rm cm}^2/{\rm g},$$

$$\kappa_{\rm R}^{\rm big} \approx \kappa_{\rm P}^{\rm big} \approx 4.6\,{\rm cm}^2/{\rm g},$$

$\mathrm{St}_0^{\rm small} \approx 3.3\times10^{-6}$ and $\mathrm{St}_0^{\rm big} \approx 3.3\times10^{-3}$ at R_0. Since we can only model one dust fluid, we assume that the small grains are perfectly coupled to the gas and their surface density is always given by $\Sigma_{\rm d}^{\rm small} = (1-X_0)\varepsilon_0\Sigma_{\rm g}$, where $X = \Sigma_{\rm d}^{\rm big}/(\Sigma_{\rm d}^{\rm small} + \Sigma_{\rm d}^{\rm big})$ is a coagulation fraction and $\varepsilon_0 = \Sigma_{\rm d}/\Sigma_{\rm g} = 0.01$ is the initial dust-to-gas ratio. The big grains are initialized with $\Sigma_{\rm d,0}^{\rm big} = X_0\varepsilon_0\Sigma_{\rm g,0}$, and evolved according to Eq. (4).

✔ それぞれの効果をON/OFFして影響を見る

- In our *fiducial* models we include all radiative terms in the energy equation Eq. (1c). The dust opacity is computed as $\kappa = (1-X_0)\kappa^{\rm small} + X_0\kappa^{\rm big}$, assuming that the redistribution of big grains does not affect the opacity.
- In models with *opacity feedback* we recalculate $X = \Sigma_{\rm d}^{\rm big}/(\Sigma_{\rm d}^{\rm small} + \Sigma_{\rm d}^{\rm big})$ at each timestep and update the dust opacity accordingly.
- In models with *backreaction* we further include the term in Eq. (6). These correspond to our most realistic models.
- As a control, we also run models with a *locally isothermal* equation of state, where we set $T = T_0$ instead of evolving Eq. (1c).

Model	EOS	X	κ feedback	backreaction
`iso`	loc. isothermal	0.9	N/A	No
`iso-b`	loc. isothermal	0.9	N/A	Yes
`rad`	radiative	0.9	No	No
`rad-o`	radiative	0.9	Yes	No
`rad-ob`	radiative	0.9	Yes	Yes
`rad-X0.99`	radiative	0.99	No	No
`rad-o-X0.99`	radiative	0.99	Yes	No
`rad-ob-X0.99`	radiative	0.99	Yes	Yes
`rad-X0.01`	radiative	0.01	No	No
`rad-o-X0.01`	radiative	0.01	Yes	No
`rad-ob-X0.01`	radiative	0.01	Yes	Yes

Fiducial モデル

- opacity feedbackもbackreactionも無い場合

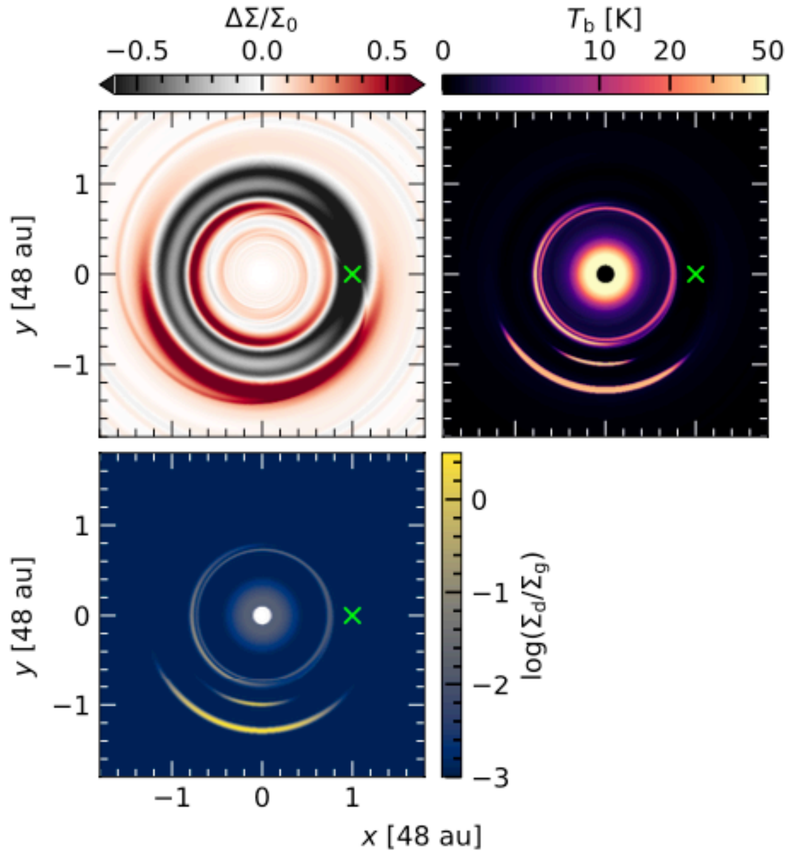

Figure 4. Perturbed gas surface density (top left), dust-to-gas ratio (bottom left), and dust brightness temperature at 1.25 mm (top right) for the fiducial model `rad` after 1100 planetary orbits. The gas shows gaps, vortices, and pressure bumps, while the dust emission shows bright crescents and rings. A green cross marks the planet's position.

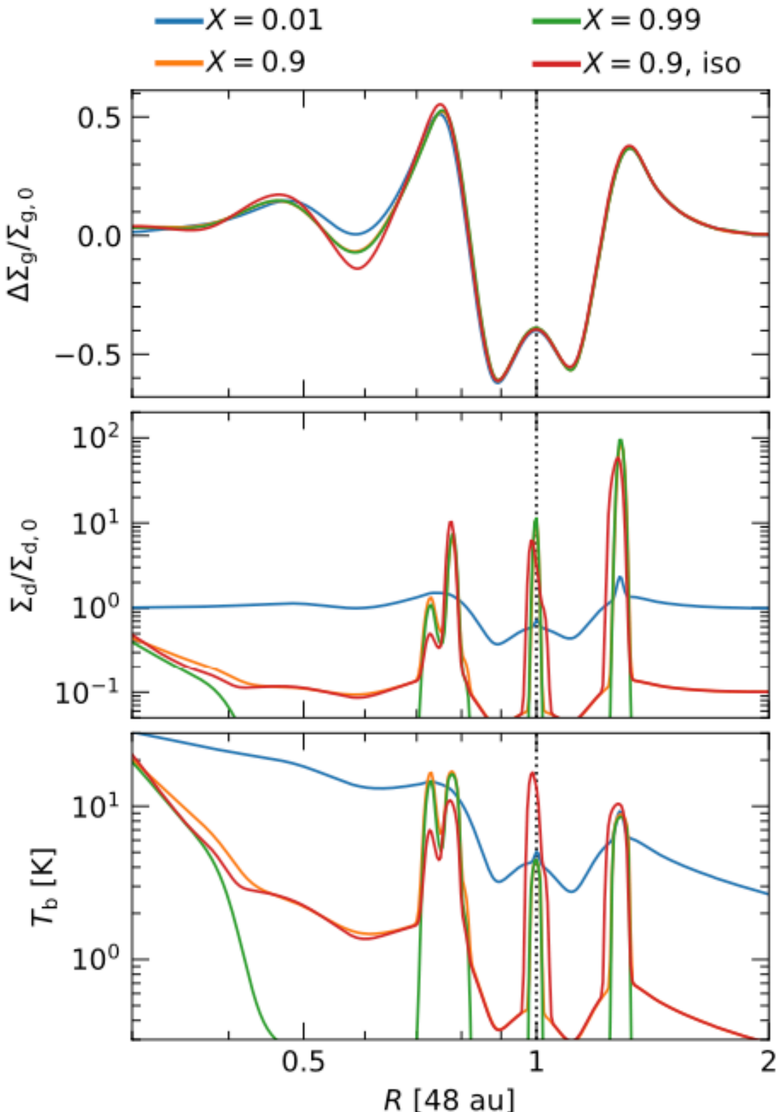

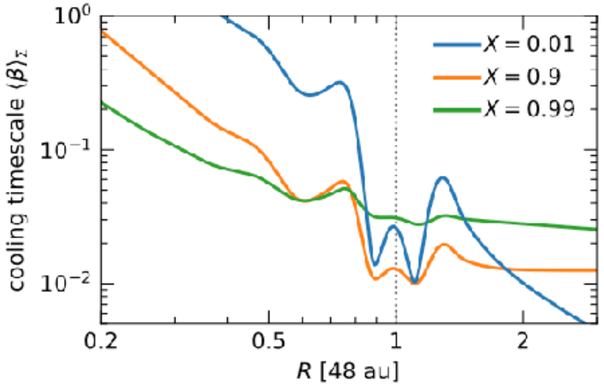

✔X=0.01 (ほぼ小さいダスト)

- ΣdがΣgに追随する
- 0.6のsecondary gap見えず
  - coolingが長いから?

✔0.9≦Xだと

- 圧力バンプにダストが溜まるので顕著な密度変化が
- X=0.9とX=0.99でほぼ変わらず

色々なモデルの比較

X=0.9

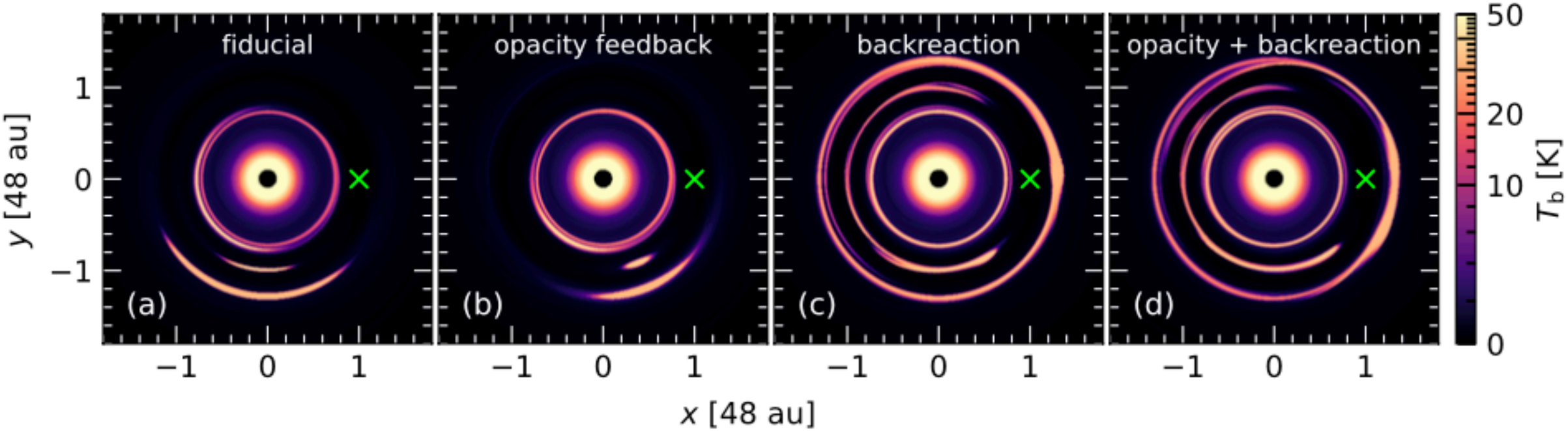

✔ opacity feedbackでよりコンパクトに、backreactionでspreadされる

- Opacity feedbackでより構造がcompactになる理由はよくわからない

  (baroclinic instability か?)

- **強い乱流をいれずとも、backreactionで構造が軸対称に向かっていく**

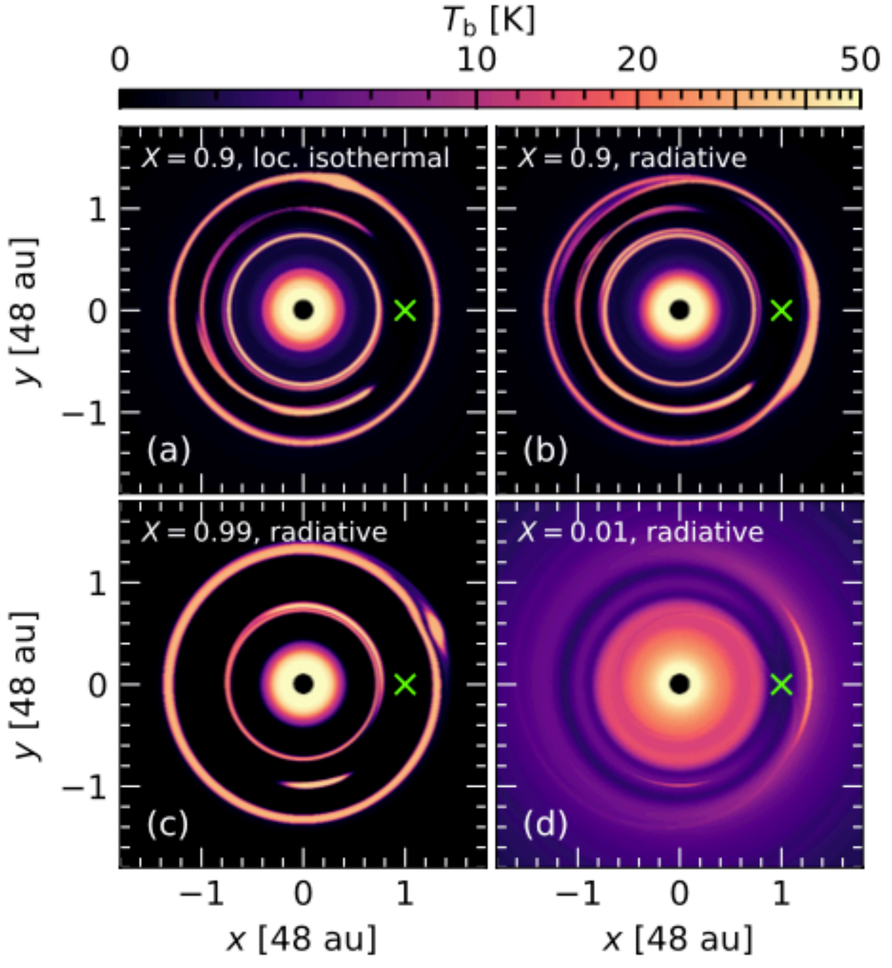

Figure 9. Similar to Fig. 7, but for models with opacity feedback and backreaction. For $X \geqslant 0.9$, (panel *b*) including these effects results in a ring rather than a vortex at the outer gap edge. For $X = 0.01$ (*d*) the results are identical to the fiducial model without feedback and backreaction in Fig. 7. A small, compact vortex is visible near the outer ring for the locally isothermal (*a*) and $X = 0.99$ (*c*) models.

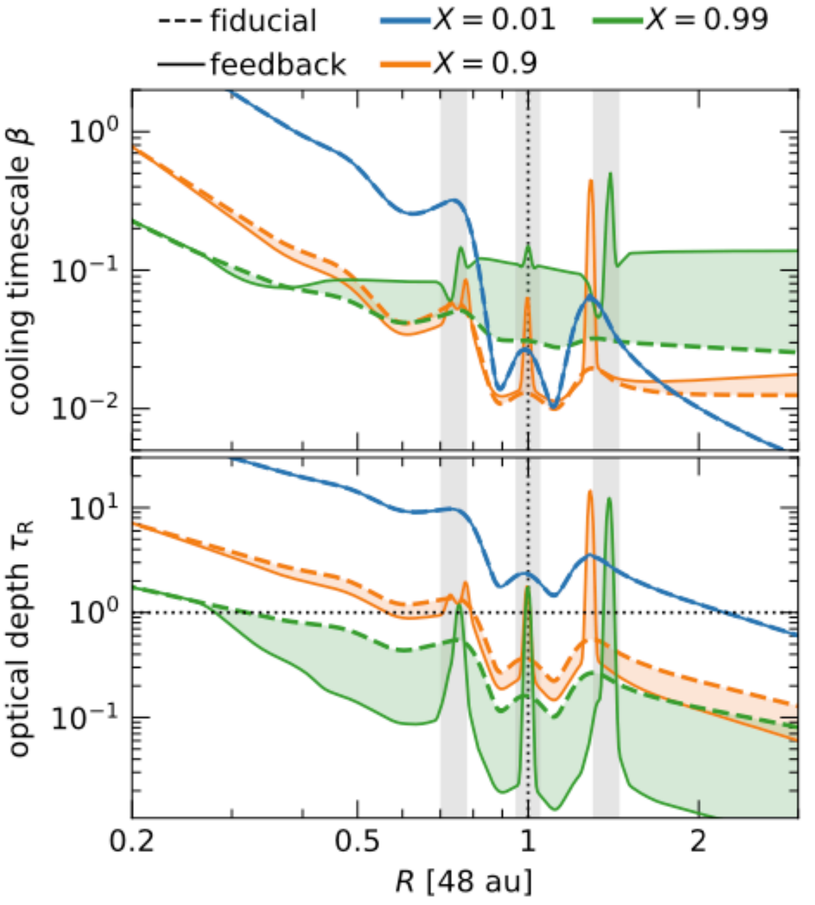

Figure 10. Density-weighted, azimuthally averaged cooling timescale β and optical depth τ_R for models with and without opacity feedback. The cooling timescale increases in the optically thin dust-depleted regions due to the lack of opacity-carrying mm grains, and near pressure bumps due to the local enhancement of the dust-to-gas ratio rendering the disk optically thick. The difference between models with and without feedback is filled in to guide the eye. Gray bands approximately mark the location of substructures.

Gaussian Process Models Impact the Inferred Properties of Giant Planets around Active Stars

QUANG H. TRAN[1] AND BRENDAN P. BOWLER[1]

[1] *Department of Astronomy, The University of Texas at Austin, 2515 Speedway, Stop C1400, Austin, TX 78712, USA*

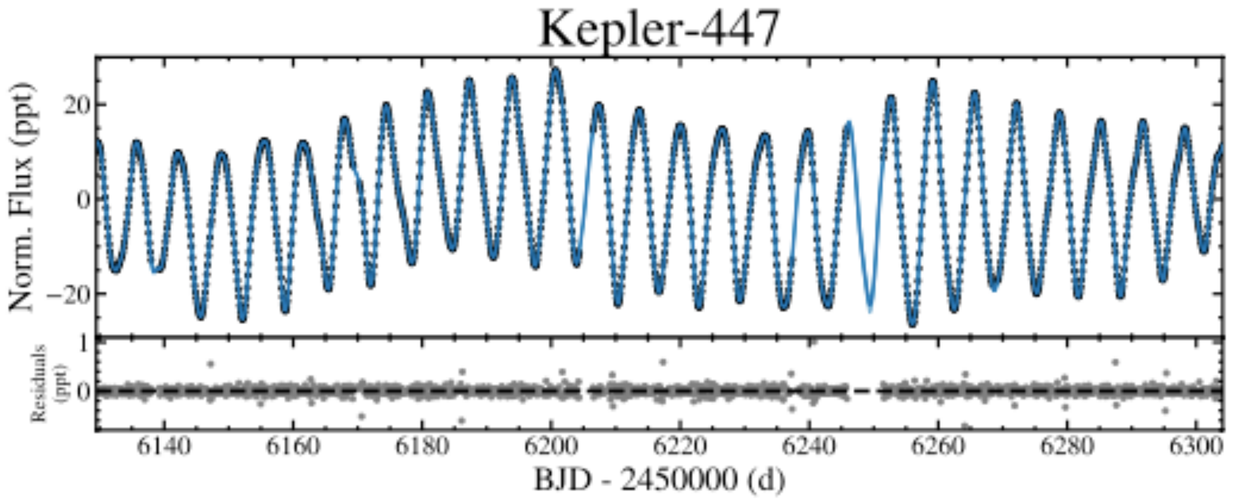

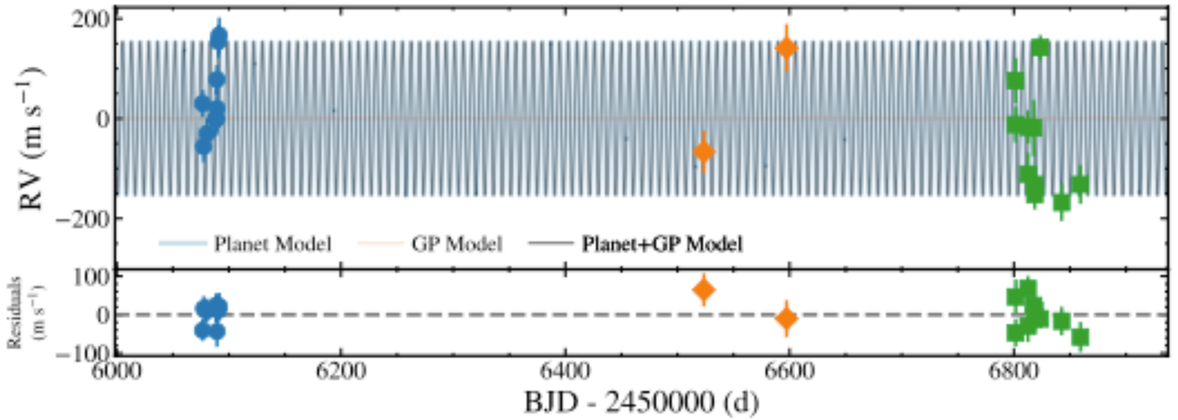

✔視線速度(RV)法での惑星の同定は、恒星活動性のシグナルとの切り分けが重要

- 恒星活動性に伴うred noiseはGaussian processなどで処理されてきた

✔本研究では、Gaussian processのパラメータを測光データから推定して

RV解析に使うとどうなるかを調べた

- RVと測光データがある17の若い天体について解析をした

ガウス過程によるトレンド除去

✔ non-parametericな回帰モデル

- 異なる時刻間の相関をカーネル関数で指定

- カーネル関数のパラメータを測光データから推定してRV解析に用いる

$$k_{\mathrm{QP}}(t,t') = A^2 \exp\left(-\frac{(t-t')^2}{2l_e^2} - \frac{\sin^2\left(\frac{\pi(t-t')}{P_{\mathrm{GP}}}\right)}{2l_p^2}\right)$$

where t and t' represent the pairs of observations in time, A is the variance amplitude, l_e encodes the evolutionary timescale, P_{GP} is the recurrence timescale (or period) of the activity signal, and l_p is the smoothness and complexity of the periodic component (or the periodic lengthscale).

Table 4. GP Hyperparameter Posteriors from Light Curve Fits

System	$\ln \sigma_{\mathrm{LC}}$			A			l_e			l_p			P_{GP}		
	MAP[a]	Median	68.3% HDI	MAP	Median	68.3% HDI	MAP	Median	68.3% HDI	MAP	Median	68.3% HDI	MAP	Median	68.3% HDI
GJ 3021	-6.8	-6.8	-6.9–-6.8	2.7	3.1	2.7–3.5	7.9	5.0	4.1–5.6	0.2	0.3	0.2–0.3	7.0	5.6	5.5–5.6
HATS-29	-27.6	-21.9	-27.6–-16.8	7.1	7.1	6.7–7.6	0.7	0.7	0.7–0.7	0.5	0.5	0.4–0.5	0.6	0.6	0.6–0.6
HAT-P-54	-4.0	-4.0	-4.0–-3.9	5.2	6.0	4.2–7.2	21.2	22.0	15.9–29.1	0.4	0.5	0.4–0.5	15.1	15.1	14.9–15.3
HD 12484	-26.2	-19.3	-27.6–-15.9	3.2	3.3	2.8–3.7	5.2	5.1	4.8–5.6	0.4	0.4	0.4–0.4	4.3	4.3	4.3–4.3
HD 102195	-3.9	-3.9	-4.0–-3.8	3.7	3.8	3.3–4.2	12.7	9.2	7.5–10.3	0.4	0.5	0.5–0.6	11.7	10.2	9.8–10.4
HD 103720	-4.4	-4.4	-4.5–-4.3	7.4	7.9	6.7–9.0	20.6	20.8	19.2–22.5	0.4	0.4	0.4–0.4	17.9	18.0	17.8–18.1
Kepler-17	-1.8	-1.8	-1.9–-1.8	2.4	2.6	2.2–2.9	11.2	10.9	9.4–12.6	0.3	0.3	0.2–0.3	12.0	11.9	11.8–12.1
Kepler-43	-4.7	-4.6	-4.8–-4.5	0.9	0.9	0.8–1.0	11.1	10.5	9.4–11.7	0.2	0.3	0.2–0.3	13.4	13.3	13.2–13.5
Kepler-75	-13.4	-13.4	-13.5–-13.3	0.5	0.5	0.4–0.6	20.7	20.3	19.0–21.7	7.5	8.0	6.5–9.3	13.8	13.9	13.6–14.1
Kepler-77	-5.3	-5.3	-5.4–-5.2	0.5	0.5	0.5–0.5	9.1	8.9	8.2–9.6	0.3	0.3	0.3–0.3	16.4	16.3	16.1–16.6
Kepler-447	-4.7	-4.7	-4.8–-4.5	8.0	8.0	7.0–8.7	7.5	7.3	6.5–7.8	0.4	0.4	0.4–0.5	6.4	6.4	5.9–6.5
Kepler-539	-4.8	-4.8	-4.9–-4.7	4.4	4.4	4.1–4.7	10.5	10.5	10.1–10.9	0.4	0.4	0.4–0.4	11.9	11.9	11.8–12.0
K2-29	-3.7	-3.7	-3.7–-3.5	5.6	5.7	5.0–6.3	10.8	10.8	10.2–11.4	0.4	0.4	0.4–0.4	10.4	10.3	10.2–10.5
K2-237	-2.3	-2.3	-2.3–-2.2	2.7	2.8	2.5–3.1	5.2	5.3	4.8–5.7	0.5	0.5	0.5–0.6	4.8	4.8	4.7–4.9
K2-250	-3.0	-3.0	-3.0–-2.9	5.6	5.9	4.9–6.6	3.0	3.0	2.9–3.1	15.6	16.1	12.5–19.4	2.3	2.3	2.3–2.4
Qatar-2	-1.8	-1.8	-1.8–-1.7	4.8	5.2	4.1–6.0	22.9	22.6	19.8–25.2	0.5	0.5	0.4–0.5	19.6	19.6	19.3–19.9
WASP-180 A	-2.5	-2.5	-2.6–-2.3	3.5	3.7	3.2–4.1	4.4	4.4	4.0–4.8	0.3	0.3	0.3–0.3	4.4	4.4	4.4–4.5

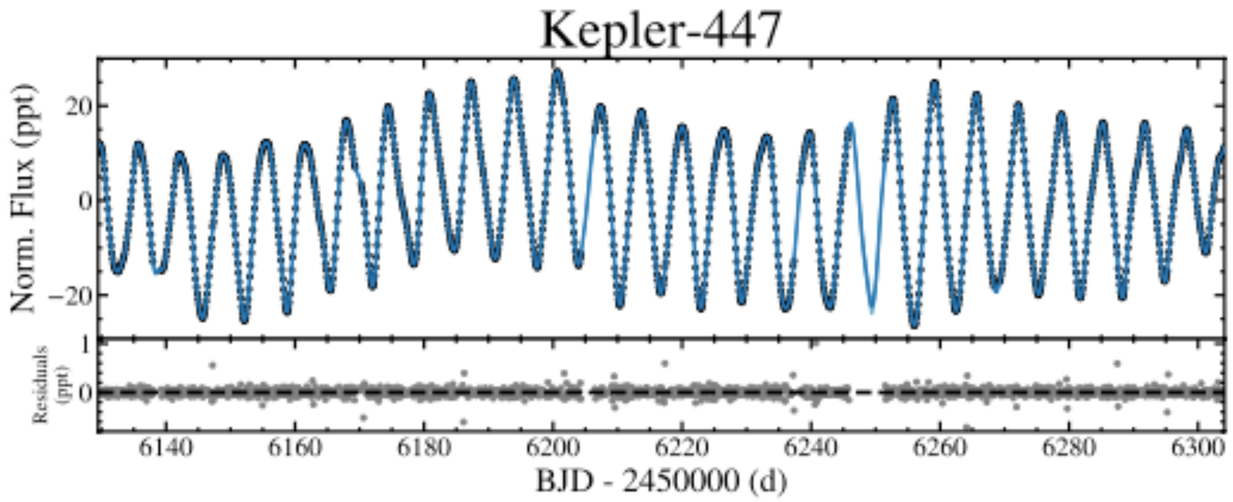

解析例

✔ 3つのモデルで比較

- orbital fitのみ
- orbital fit + GP
- orbital fit + GP
  (GPはLCから決定)

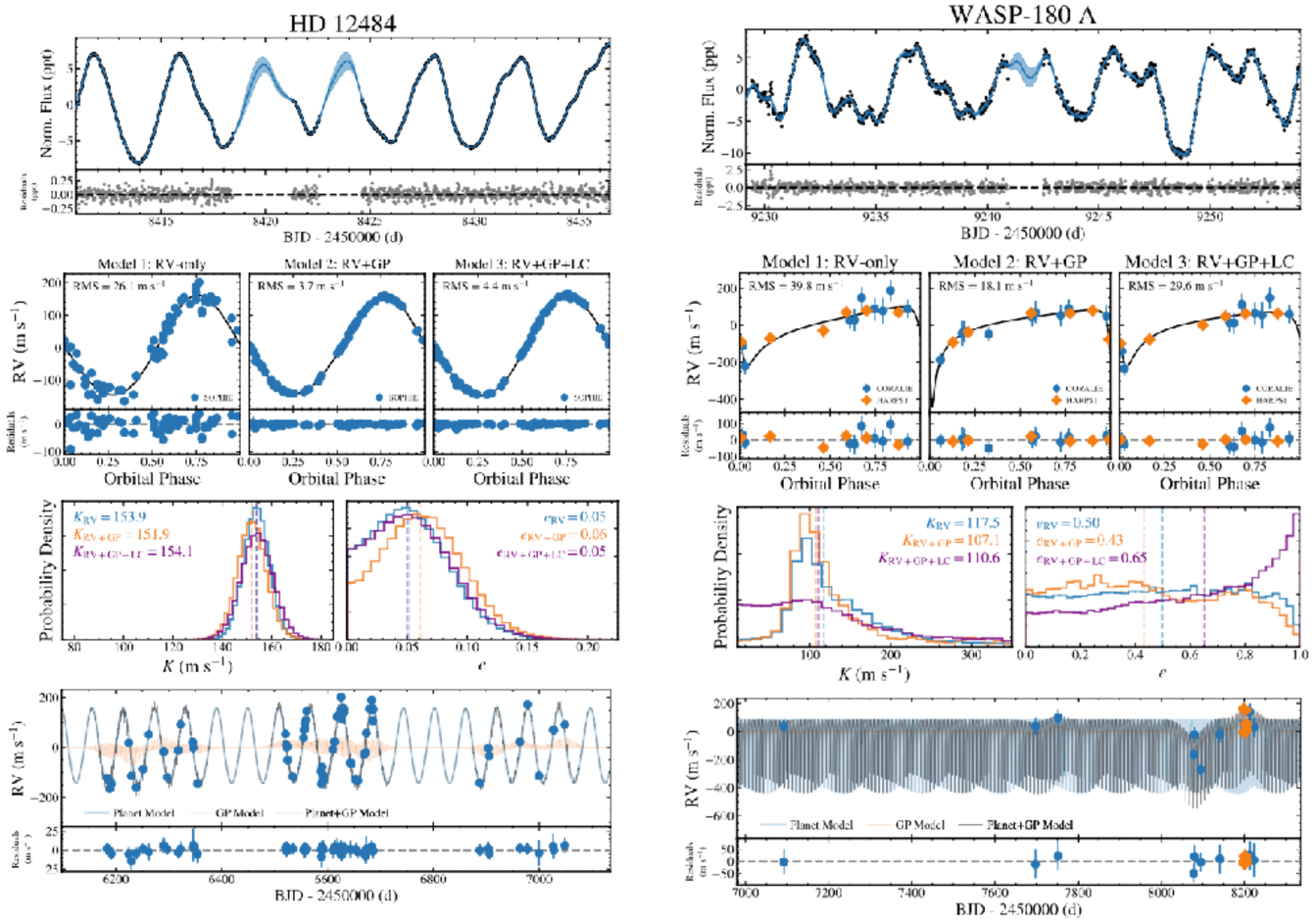

Model	T_0	P	$\sqrt{e}\sin\omega$	$\sqrt{e}\sin\omega$	e	ω^a	K	A	l_e	l_p	$P_{\rm GP}$
	(BJD - 2450000)	(d)				(°)	(m s^{-1})	(m s^{-1})			(d)
HD 12484											
Model 1	$6698.49^{+0.76}_{-0.71}$	$58.853^{+0.074}_{-0.074}$	$-0.07^{+0.12}_{-0.14}$	$0.17^{+0.11}_{-0.08}$	$0.05^{+0.03}_{-0.04}$	$303.48^{+56.52}_{-130.84}$	$153.9^{+5.2}_{-5.2}$	...	...	...	...
Model 2	$6698.17^{+0.82}_{-0.80}$	$58.840^{+0.080}_{-0.075}$	$0.00^{+0.15}_{-0.15}$	$0.20^{+0.10}_{-0.08}$	$0.06^{+0.03}_{-0.04}$	$144.20^{+175.79}_{-144.20}$	$151.9^{+5.8}_{-5.8}$	$12.7^{+6.0}_{-9.1}$	$29.35^{+20.65}_{-8.84}$	$24.26^{+9.22}_{-24.26}$	$24.36^{+9.30}_{-24.31}$
Model 3	$6698.52^{+0.81}_{-0.76}$	$58.836^{+0.082}_{-0.081}$	$-0.04^{+0.13}_{-0.16}$	$0.17^{+0.12}_{-0.09}$	$0.05^{+0.03}_{-0.04}$	$286.91^{+73.09}_{-219.53}$	$154.1^{+6.5}_{-6.5}$	$24.9^{+6.6}_{-5.0}$	$5.11^{+0.40}_{-0.40}$	$0.39^{+0.02}_{-0.02}$	$4.28^{+0.02}_{-0.02}$
WASP-180 A											
Model 1	$7763.23^{+1.43}_{-0.50}$	$3.786^{+0.583}_{-0.410}$	$0.37^{+0.52}_{-0.35}$	$-0.25^{+0.41}_{-0.49}$	$0.52^{+0.45}_{-0.20}$	$130.06^{+63.44}_{-77.77}$	$122.4^{+69.8}_{-53.5}$	...	...	...	...
Model 2	$7763.14^{+0.64}_{-1.12}$	$3.791^{+0.408}_{-0.503}$	$0.43^{+0.54}_{-0.28}$	$-0.15^{+0.43}_{-0.50}$	$0.53^{+0.44}_{-0.21}$	$119.63^{+58.59}_{-78.84}$	$115.0^{+54.8}_{-49.8}$	$109.4^{+53.7}_{-70.7}$	$28.72^{+21.28}_{-7.81}$	$26.75^{+23.21}_{-9.48}$	$24.58^{+12.78}_{-21.49}$
Model 3	$7763.24^{+0.74}_{-1.20}$	$3.814^{+2.099}_{-1.531}$	$0.03^{+0.74}_{-0.51}$	$-0.17^{+0.38}_{-0.78}$	$0.67^{+0.33}_{-0.21}$	$175.08^{+105.59}_{-110.75}$	$109.7^{+49.0}_{-106.5}$	$83.7^{+38.4}_{-44.4}$	$4.40^{+0.38}_{-0.38}$	$0.30^{+0.02}_{-0.02}$	$4.44^{+0.04}_{-0.03}$

パラメータ推定の比較

1. Constraints on physical and orbital planetary properties can vary dramatically: by as much as 67% in minimum planet mass and 95% in eccentricity between different implementations of stellar activity models. These differences are greater than the median measurement uncertainties for these parameters (7% and 69%, respectively).

As part of this analysis, we compare the inferred QP kernel parameters from a GP model trained on photometry with parameters determined from RVs alone. We find that high-cadence RV sampling is necessary to robustly measure the stellar rotation period with a GP model trained only on RV data. For one of our systems where this constraint was possible (GJ 3021), we found that the inferred stellar rotation period is in reasonably good agreement with the stellar rotation period derived from a GP model fit to the photometry given the gap in observations.